ACS APPLIED MATERIALS & INTERFACES

www.acsami.org

Research Article

Crystalline Semiconductor Boron Quantum Dots

Jinqian Hao, Guoan Tai,* Jianxin Zhou, Rui Wang, Chuang Hou, and Wanlin Guo*

Cite This: *ACS Appl. Mater. Interfaces* 2020, 12, 17669−17675

Read Online

ACCESS | Metrics & More | Article Recommendations | Supporting Information

ABSTRACT: Zero-dimensional boron structures have always been the focus of theoretical research owing to their abundant phase structures and special properties. Boron clusters have been reported extensively by combining structure searching theories and photoelectron spectroscopy (PES) experiments; however, crystalline boron quantum dots (BQDs) have rarely been reported. Here, we report the preparation of large-scale and uniform crystalline semiconductor BQDs from the expanded bulk boron powders via a facile and efficient probe ultrasonic approach in the acetonitrile solution. The obtained BQDs have 2.46 nm average lateral size and 2.81 nm thickness. Optical measurements demonstrate that a strong quantum confinement effect occurs in the BQDs, implying the increase of the band gap from 1.80 eV for the corresponding bulk to 2.46 eV for the BQDs. By injecting the BQDs into poly(vinylpyrrolidone) as an active layer, a BQD-based memory device is fabricated that shows a rewriteable nonvolatile memory effect with a low transition voltage of down to 0.5 V and a high on/off switching ratio of 10^3 as well as a good stability.

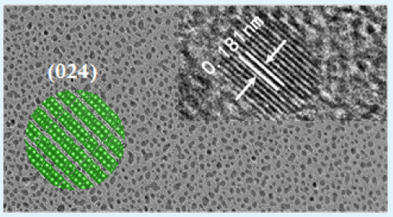

KEYWORDS: *boron, quantum dots, quantum confinement effect, ultrasound, nonvolatile memory device*

Downloaded via NANJING UNIV AERONAUTICS & ASTRNTCS on May 7, 2020 at 09:23:38 (UTC).
See https://pubs.acs.org/sharingguidelines for options on how to legitimately share published articles.

1. INTRODUCTION

Elemental boron, at the critical position of metallic and nonmetallic elements, has three valence electrons and exhibits multicenter bonding character owing to the electron deficiency with both classical two-center, two-electron and novel three-center, two-electron B−B bonds.[1−6] The unusual bonding situation makes the bulk boron to have at least 16 polymorphs that have robust stiffness, strength, toughness, and stability for potential applications in advanced high-temperature devices.[2,7] In contrast, low-dimensional boron nanostructures are expected to have wider applications than the bulk counterpart.[7−9] To date, zero-dimensional (OD) boron cage molecules (boron clusters), one-dimensional (1D) nanowires and nanotubes, and two-dimensional (2D) sheets or nanofilms have been extensively reported experimentally and theoretically.[7−17] However, crystalline boron quantum dots (BQDs) are rarely reported experimentally.

After the discovery of buckminsterfullerene (C_{60}),[18] a series of crystalline metal oxide and semiconducting quantum dots/nanoparticles were synthesized to boom the various investigations on dramatically chemical and physical properties towards wider applications in nanoscale sensors, random lasers, and highly efficient energy conversion and storage devices.[19−23] Boron is also able to form sp^2 and sp^3 bonding and thus is regarded as the best candidate after carbon to form C_{60}-like structures and quantum dots.[3] In the past decade, it has been predicted and proved by combining CALYPSO structure searching theories and photoelectron spectroscopy (PES) experiments that the structure and chemical bonding of boron nanoclusters, B_n, strongly depend on the nanocluster size.[24−28] Especially, the long-sought B fullerene analogue (borospherenes) was found at B_{40} with a large highest occupied molecular orbital−lowest unoccupied molecular orbital (HOMO−LUMO) gap of more than 5.0 eV.[29] Despite these advances, crystalline BQDs have been rarely prepared. Therefore, it is an urgent need to develop a facile preparation method for large-scale and high-quality crystalline BQDs.

In this work, crystalline semiconductor BQDs have been successfully synthesized by a probe ultrasonic procedure using the expanded boron powders as the raw material in a highly polar organic solvent of acetonitrile. Crystal structures and surface morphologies of the BQDs were tested by high-resolution transmission electron microscopy (HRTEM) and atomic force microscopy (AFM), and their optical properties were analyzed by photoluminescence and UV/vis absorption spectroscopies. To demonstrate the device application, a BQD-based nonvolatile memory device was fabricated, wherein the BQDs are the materials for charge trapping in the nonvolatile device. This work would pave the novel avenues for applications of zero-dimensional boron materials in photoelectronics and energy storage and memory devices.

2. EXPERIMENTAL SECTION

2.1. Materials. Acetonitrile (99.7%) and *N*-methyl-pyrrolidone (NMP) (99.7%) were purchased from China National Pharmaceutical Group Corporation. Poly(vinylpyrrolidone) (PVP, MW = 130 000) was obtained from Sigma-Aldrich Chemie GmbH (Sternheim,

Received: October 30, 2019
Accepted: March 23, 2020
Published: March 23, 2020

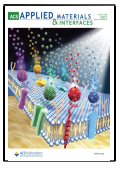

ACS Publications © 2020 American Chemical Society

https://dx.doi.org/10.1021/acsami.9b19648
ACS Appl. Mater. Interfaces 2020, 12, 17669−17675

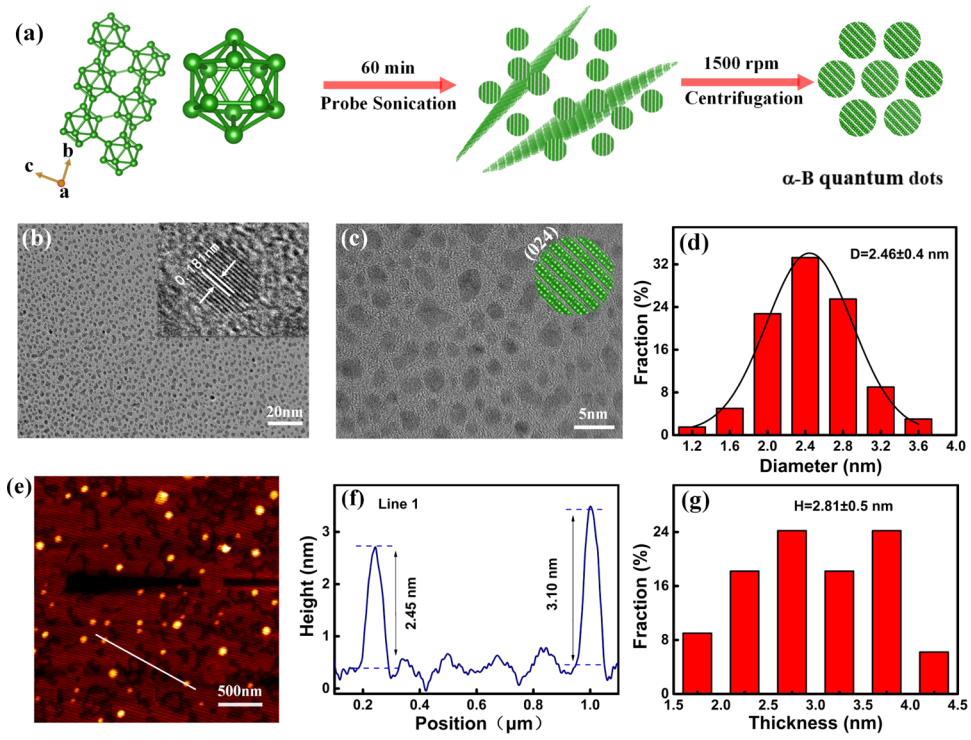

Figure 1. Preparation and structural characterization of the crystalline semiconductor BQDs. (a) Schematic diagram of preparing the BQDs from the expanded boron powder. (b) Low-magnification TEM image of the BQDs. The inset shows a typical HRTEM image of individual BQD with a lattice spacing of 0.181 nm. (c) HRTEM image of the BQDs. The inset shows the atomic structure of the BQD along the (024) orientation related to the inset of (b). (d) Lateral size distribution of BQDs obeys a Gaussian distribution. (e) AFM image of the BQDs on a mica substrate. (f) Thickness profile of the BQDs along the white line in (e). (g) Thickness distribution of the BQDs, indicating that the average thickness is around 2.81 nm.

Germany). Expanded boron powder (99.999%) was received from Aladdin Reagent Corporation. All of the materials were used without purification. In a typical preparation of BQDs, 30 mg of boron powder was first added into a three-necked bottle and then 15 mL of acetonitrile was added into the bottle before the probe ultrasonication process. The preparation was performed at an output power of 400 W and an ultrasonic time of 60 min. The diameter of the probe composed of a titanium alloy is 10 mm, and the frequency was controlled at 20 kHz. To avoid overheating of the solution under ultrasound, we designed a simple cooling cycle device to keep the system at a constant temperature. The resultant solution was centrifuged at 1500 rpm for 60 min. The supernatant containing BQDs was extracted gently. All of the experiments were conducted at room temperature.

2.2. Characterization. Transmission electron microscopy (TEM) images and selected area electron diffraction (SAED) patterns were obtained using an FEI Talos F200 S field-emission transmission electron microscope with an operating voltage of 200 kV. An atomic force microscope (AFM, Bruker Dimension Edge) was used to obtain the thickness and size of the as-prepared boron quantum dots (BQDs) in tapping mode in air. Raman and photoluminescence (PL) spectra were performed using a laser confocal Raman spectrometer (LabRAM HR Evolution, HORIBA Jobin Yvon, France) with a 325 nm He−Ne laser at room temperature. The characteristic peak of a silicon wafer located at 520 cm^{-1} was utilized to calibrate the Raman spectrometer. The X-ray photoelectron spectroscopy (XPS) spectra were measured on a Thermo Scientific spectrometer (ESCALAB 250Xi) equipped with a pass energy of 30 eV and an X-ray source ($h\nu$ = 1486.65 eV) with monochromatized Al Kα. All of the samples were tested under a low pressure down to 1.0×10^{-9} Pa, and the spectra were analyzed using Advantage software with an energy step of 0.05 eV. SEM images were investigated by a field-emission scanning electron microscope (FEI Nova 450). X-ray diffraction (XRD) measurement was performed on a Japanese Science Smartlab9 with a tube voltage of 40 kV and a tube current of 150 mA. UV−vis spectra were recorded on a UV-3600 spectrophotometer at room temperature. The time-resolved PL (TRPL) experiment was obtained by an FLS1000 photoluminescence spectrometer.

2.3. Fabrication of BQD-PVP-Based Memory Devices. First, after the treated dispersion was centrifuged at a speed of 1500 rpm for 60 min, the supernatant containing the BQD suspension of 5 mL was centrifuged at a speed of 10 000 rpm for 30 min. Second, the BQD was collected and redispersed in NMP of 1 mL and the PVP particles were also dissolved in NMP of 1 mL. Third, the two dispersion solutions were mixed to produce a mixture composed of BQDs and PVP, which is referred to as BQD-PVP. Fourth, the mixture was sonicated for 30 min in an ultrasonic cleaning machine. Fifth, a glass substrate with prefabricated Au line electrodes was prepared using a shadow mask by a magnetron sputtering equipment, where the thickness, width, length, and the distance among the electrodes are 110 nm, 0.5, 25, and 1.5 mm, respectively. Sixth, the film was deposited on the glass substrate by spin coating at a speed of 800 rpm for 20 s and then 1500 rpm for 40 s. Seventh, after the film was heated at 60 °C for 1 h at a hot stage, Ag line electrodes with 80 nm in thickness, 0.5 mm in width, and 25 mm in length are deposited by the magnetron sputtering process. The top Ag and bottom Au electrodes are perpendicular. Finally, 8 × 8 device arrays with the active layer BQD-PVP were fabricated. The nonvolatile memory device with a sandwich configuration refers to glass/Au/BQD-PVP/Ag. *I*−*V* characteristic was measured by a source measurement unit system (Keithley 2400) at room temperature.

3. RESULTS AND DISCUSSION

A feasible probe sonication process was employed to prepare the BQDs in acetonitrile solution, as shown in Figure 1a. The BQDs were obtained by sonicating the boron powders for 60 min and then centrifuging at 1500 rpm for 60 min. We employed expanded boron powders with layered structures (Figure S1), which resulted in the formation of BQDs under high-intensity probe ultrasonic treatment. The dipole−induced dipole interaction is regarded as an important cause for dispersing

https://dx.doi.org/10.1021/acsami.9b19648
ACS Appl. Mater. Interfaces 2020, 12, 17669−17675

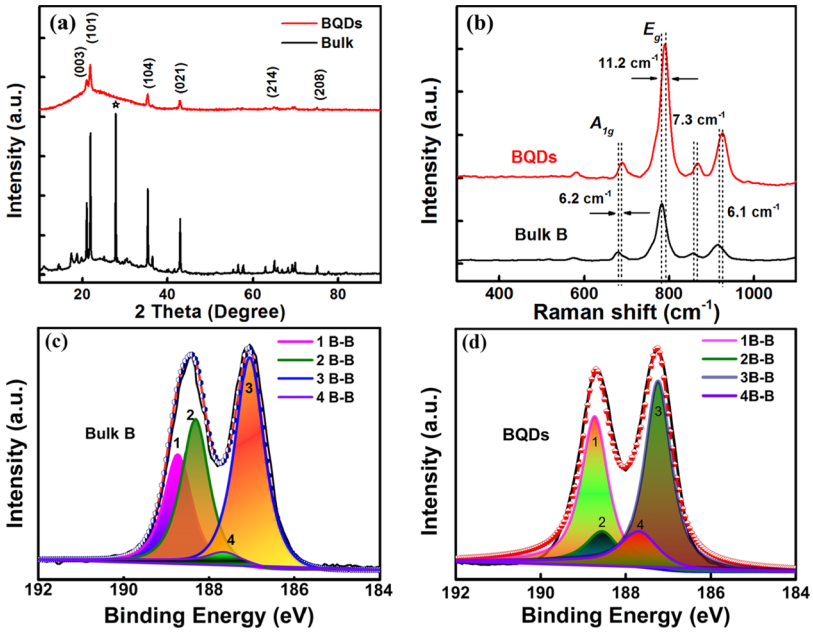

Figure 2. XRD, Raman, and XPS characterizations of the BQDs. (a) XRD patterns of the BQDs (red line) and bulk boron (black line); the peak marked by * can be indexed to carbon (PDF 22-1069). (b) Raman spectra of the BQDs and the bulk counterpart irradiated by BQDs by a 325 nm laser, where the blue shift of the peaks (E_g and A_{1g}) of the BQDs in comparison with the bulk indicates that the BQDs are ultrasmall and ultrathin. High-resolution XPS spectra of B_{1s} core-level electrons of boron powder (c) and BQDs (d).

nanomaterials in some highly polar solvents such as the preparation of graphene quantum dots (GQDs) using disperse expended graphite in a polar solvent under ultrasound,[30] so a similar effect may occur between the expanded boron powders with a layered structure and the polar acetonitrile solvent.

The structure of BQDs is analyzed by field-emission transmission electron microscopy (TEM) and high-resolution atomic force microscopy (AFM). The TEM images of BQDs indicate that a large quantity of ultrasmall and uniform BQDs have been prepared (Figure 1b,c). The high-resolution TEM (HRTEM) images show that the BQDs with highly paralleled lattice fringes are well-crystallized (Figure 1c). The lattice distance of BQDs was measured to be 0.181 nm (inset of Figure 1b), which is in good agreement with the (024) lattice spacing of a α-rhombohedral boron structure (PDF 78-1571), indicating that quantum dots are derived from α-rhombohedral boron. The BQDs with good reproducibility can be prepared many times, as shown in Figure S2. According to statistical analysis of 400 quantum dots, it is shown that the average lateral size of the BQDs is 2.46 $\pm$ 0.4 nm and the diameter of more than 80% BQDs is in the range from 2 to 2.8 nm that conforms to the Gaussian fitting distribution curve (Figure 1d). To further verify the thickness of the as-synthesized BQDs, an AFM image was obtained, as shown in Figure 1e. The thickness profile from the AFM data reveals that the thicknesses of BQDs are 2.45 and 3.10 nm for two different BQDs, which respectively correspond to the number of periodic lattices of the BQDs with around five and seven layers[31] (Figure 1f). Statistical AFM analysis shows that the BQDs with 2.81 $\pm$ 0.5 nm in average thickness (Figure 1g) correspond to 6 $\pm$ 1 in the number of boron layers. All of the above results demonstrate that the ultrathin and ultrasmall BQDs have been successfully prepared in the acetonitrile solution by the probe ultrasonic treatment.

The crystal structure of as-synthesized BQDs was systematically investigated by XRD measurements (Figures 2a and S3). Figure 2a shows typical XRD profiles for the original boron powder and as-prepared BQDs, which can be indexed into α-rhombohedral boron (PDF 78-1571). Compared to that of the commercial boron powder, the XRD peak intensity of the BQDs decreases sharply and the peak of the (101) reflection was broadened at around 22°, which demonstrates the highly dispersed structure of these BQDs. In addition, a peak marked by * can be indexed to carbon (PDF 22-1069), which is attributed to the carbon impurities in the bulk boron. Theoretically, if a material is monolayer which would no interaction happening among the layers, weak or no diffraction peak would be detected in the XRD pattern which corresponds to the *d*-spacing of the layered crystals.[32,33] After the ultrasonic treatment, the disappearance of most of the peaks in the XRD pattern of the BQDs results from the reduced crystallinity of ultrasmall and ultrathin BQDs and the interlayer interaction upon the dispersion process, similar to the dispersion of boron nitride quantum dots (BNQDs).[34] Consequently, the XRD result further verifies that the BQDs are a few layers in thickness and ultrasmall in size, which is in good agreement with the experimental results of TEM and AFM measurements in Figure 1.

Raman spectroscopy is utilized to investigate the structure and crystallinity of the BQDs and the bulk counterpart (Figures 2b and S4). It is observed that there are two prominent bands of the BQDs located at 687.2 and 792.8 cm^{-1}, as shown in Figure 2b. The two bands can be attributed to one in-plane phonon mode (A_{1g}) located at 687.2 cm^{-1} and the other out-of-plane vibration mode (E_g) at 792.8 cm^{-1}.[35] In contrast, the Raman spectrum of the corresponding bulk powder shows significant blue shifts of the A_{1g} and E_g bands of around 6.4 and 11.2 cm^{-1}, respectively. This phenomenon was also observed in previous reports about BNQDs[33] and black phosphorus QDs (BPQDs).[36]

To further probe the surface composition and chemical state of the samples before and after the probe sonication treatment, X-ray photoelectron spectroscopy was utilized (Figure 2c,d).

https://dx.doi.org/10.1021/acsami.9b19648
ACS Appl. Mater. Interfaces 2020, 12, 17669−17675

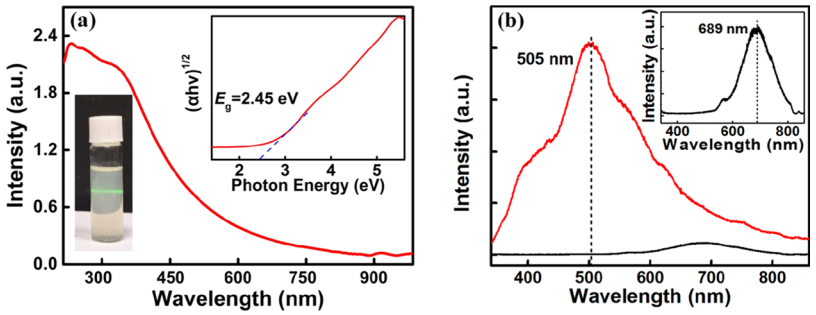

Figure 3. Optical characterizations of the BQDs. (a) UV−vis spectrum of the BQDs. The inset shows the corresponding photograph of the BQDs dispersed in acetonitrile under visible light irradiation. (b) PL spectra excited by a 325 nm laser, where red and black lines represent the BQDs and the boron powder, respectively. The inset corresponds to the magnified PL spectrum of the boron powder.

The XPS survey-scan spectra of BQDs and boron powder are shown in Figure S5. In addition to the B band, the bands corresponding to N, C, and O were also detected. It is generally considered that the C and N bands may originate from impurities from the external environments because the samples are inevitably exposed to air before the measurements. In addiiton, the excess C species also come from the impure introduction of the bulk powder, which has been confirmed by Rama spectrum (Figure S4). Figure 2c,d shows the high-resolution B_{1s} core-level electrons of the boron powder and the BQDs, respectively. The spectrum of BQDs is fitted into four characteristic peaks: 187.1, 187.6, 188.3, and 188.5 eV, respectively. All of the peaks correspond to the B−B band,[37] which indicate that the crystal structure of boron remains intact after the probe ultrasonic treatment. In comparison with the XPS peaks of the boron powder, the main peaks of the BQDs are red-shifted slightly and the trend is consistent with the reported phenomenon observed in 2D boron sheets.[37] This result further confirms the formation of BQDs after ultrasonicating the boron powder in the acetonitrile solution.

To confirm the optical band gap of the as-synthesized BQDs, the UV−visible absorption spectrum of the BQDs was performed (Figure 3a). From the absorption spectrum, the optical band gap can be calculated via the Tauc plot formula.[38] The equation is given as $\alpha = A(E - E_g)^{1/n}/E$, where A is a constant, α is the absorption coefficient, E_g is the optical band gap, and E is the photon energy. For indirectly allowed transition, $n = 2$, namely, $(\alpha h\nu)^{1/2} = h\nu - E_g$ (inset, Figure 3a). The calculated optical band gap E_g is estimated to be 2.45 eV, which is higher than that of the corresponding bulk of around 1.80 eV (Figure S6), indicating the occurrence of a significant quantum confinement effect in the BQDs. The as-synthesized BQDs, showing a light brown phase, can be dispersed in the acetonitrile solution (the inset at the bottom left of Figure 3a). The solution is very stable at room temperature for more than three months without any noticeable aggregation, which is determined by the Tyndall effect.

Furthermore, the room-temperature PL spectra of the BQDs and the boron powder are used to characterize the optical properties, where the red and black lines refer to the PL spectra of the BQDs and the boron powder, respectively (Figures 3b and S7). The room-temperature PL spectrum of the BQDs shows a broadened and strong emission band centered at 505 nm (the photon energy is 2.46 eV). The measured PL peak position of the boron powder is 689 nm (the photon energy is 1.80 eV) (the inset of Figure 3b). In good consistence with the UV/vis spectrum, the remarkable blue shift of around 184 nm in the PL spectra is detected and can be attributed to the significant quantum size effect in the BQDs. Additionally, the broadened emission peak is similar to the observation in the GQDs resulting from the ultrasmall size and surface defect edge.[39]

To explain the PL mechanism of the BQDs, the time-resolved PL (TRPL) spectroscopy was performed. The fluorescence lifetimes of the BQDs and the boron powder are shown in Figure S8. The fluorescence decay curve of BQDs indicates two exponential decays with fast (1.36 ns, 75.32%) and slow (9.29 ns, 24.68%) decay components, which correspond to recombinations from the intrinsic and defect-induced states, respectively. This experimental result is similar to the measured exciton and localized states in BNQDs[34] and GQDs[39] as well as the traditional semiconductors such as Si and ZnO nanocrystals.[21,23] The decay curve clearly indicates that the emission from intrinsic states shows a shorter recombination lifetime than that from defect states. Therefore, we can reasonably conclude that under the laser excitation with a wavelength of 325 nm the main part of the emission originates from the intrinsic state of the BQDs, while the small part of the emission is attributed to the defect states because of the presence of vacancies or interstitial atoms.

The preparation process of quantum dots was investigated by performing additional experiments indicated as below: the effect of the ultrasonic time and ultrasonic powers on the size of the BQDs was probed. The BQDs were marked as BQDs-1, BQDs-2, BQDs-3, and BQDs-4 for the quantum dots synthesized at 400 W for 1 h, 400 W for 2 h, 550 W for 1 h, and 400 W for 4 h, respectively. Then, the BQDs were obtained by centrifuging the supernatant containing BQDs at a rate of 1500 rpm for 1 h. The obtained small-particle-size BQDs with the calculated average lateral size of 2.46 ± 0.4 nm for BQDs-1 (Figures 1d), 2.32 ± 0.4 nm for BQDs-2, 1.58 ± 0.2 nm for BQDs-3, and 5.8 ± 0.8 nm for BQDs-4 (Figure S9), respectively. It is obviously noticed that the size of the BQDs decreases more apparently with the increase of the sonication power than the extension sonication time according to the TEM results and the size distribution images (Figures 1 and S9). For prolonging the ultrasonic time up to 4 h, it is found that the average lateral size is increased to 5.8 ± 0.8 nm, as analyzed from the size distribution curve of the BQDs. This phenomenon is also observed in the synthesis of GQDs, so we can deduce that the BQDs-4 are produced at early stages in the acetonitrile solvent under the probe ultrasonic treatment and then the BQDs-4 rapidly appear to aggregate again to reassemble the larger nanoparticles due to the strong thermal effect from the high energy generated during the prolonged probe sonication.[39] From the HRTEM images, all of the BQDs have a lattice-fringe spacing of 0.181 nm, which corresponds to the (024) lattice fringes of the α-rhombohedral B structure (PDF 78-1571). Furthermore, the standard XRD

https://dx.doi.org/10.1021/acsami.9b19648
ACS Appl. Mater. Interfaces 2020, 12, 17669−17675

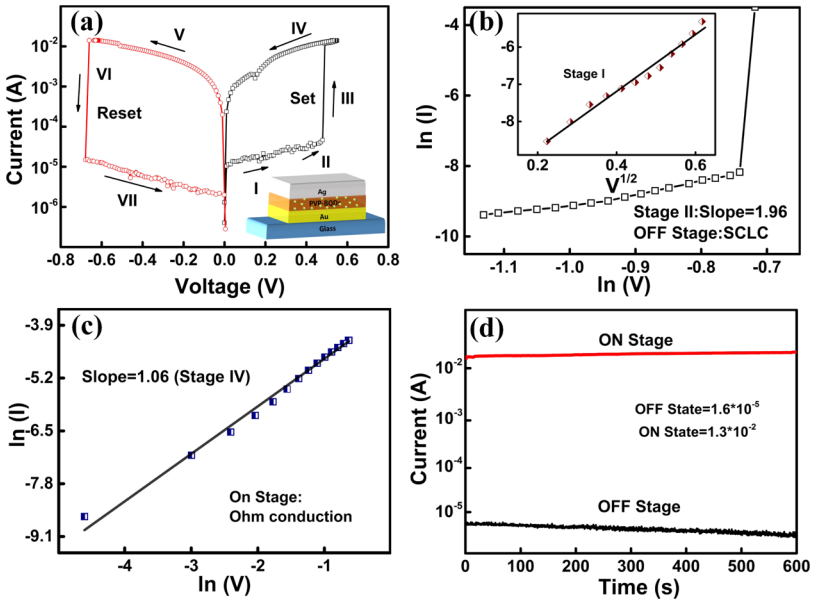

Figure 4. Properties of the BQD-based nonvolatile memory device. (a) $I-V$ characteristics of the BQD-based device. The inset shows the schematic diagram of the device. (b) Fitted lines of experimental data in the off state. Hollow dots correspond to the experimental data. (c) Fitted line of experimental data in the on state. (d) Maintain-ability measurement of the BQD-based nonvolatile device with a reading voltage of 0.1 V under the on and off states.

diffraction pattern of α-rhombohedral boron is shown in Figure S3. Compared with those of BQDs-1, the quality and crystallinity of BQDs-2 and BQDs-3 with a smaller size (inset of Figure S9) are relatively low. Therefore, the above characterizations are all mainly for the BQDs-1 and the fundamental device application of as-synthesized BQDs-1 is also further investigated in the following section.

To evaluate the device application potential of the BQDs, we fabricated a rewriteable nonvolatile memory devices with a sandwich configuration of glass/Au/BQD-PVP/Ag, where the BQD-PVP were selected as an active layer for the memory device (Figure 4). Previously, C_{60},[40] black phosphorus,[36] and GQDs[41] composited in polymers have been extensively studied in the organic−inorganic hybrid nanomaterials with a distinctive resistance-switching effect for emerging data storage devices. As a potential application, we describe a nonvolatile memory effect of the BQD/PVP-based device. The BQD-based memory device displays an electrical bistability (Figure 4a). It is observed that in the device starting with the low-conductance state (LCS) the current slowly increases with the applied positive voltage (stage I, off state). Nevertheless, the current shows an abrupt increase from 1.6×10^{-5} (stage II) to 1.3×10^{-2} with a high-conductance state (HCS, stage III, on state) when the applied positive voltage increases up to about 0.5 V, which demonstrates that the switching characteristic of the device transforms from LCS to HCS. The electrical transformation from the LCS to the HCS is identical to a set/write process in nonvolatile devices. The device exhibits a high stability in the HCS during the subsequent voltage scan (stage IV) and can be maintained when turning off the electrical power, indicating that such a device has a rewriteable nonvolatile memory characteristic. After applying a negative voltage of −0.7 V (stage VI), the device can be returned to the LCS state again, which is identical to the reset/erase process of the device. During the subsequent negative voltage scan, the memory device remains in the LCS (stage VII). Such write (set)/erase (reset) processes have been cyclically tested many times, and no considerable degradation was observed. This rewriteable nonvolatile feature allows the application of BQD-PVP nanocomposites in the advanced flash memory device.

To further understand the device operating mechanism, the experimental and fitting curves of $I-V$ are analyzed using the theoretical space-charge-limit current (SCLC) model. Four visible stages are noticed in the $I-V$ curve during the positive voltage sweep (Figure 4a). As can be seen from the inset of Figure 4b, the curve of $\ln(I)$ vs $V^{1/2}$ in the voltage range from 0 to 0.4 V can be fitted as a straight line (stage I, off state). The linear feature suggests that the conductive mechanism can be attributed to the thermionic emission,[42] which results from PVP as an insulating polymer with a large barrier. The conduction is dominantly originating from the charge injection from the electrode to the BQD-PVP active layer. In stage II, a linear relation is observed in the plot of $\ln(I)$ and $\ln(V)$ for the voltage sweep from 0.4 to 0.5 V with a slope of 1.96 (Figure 4b), which indicates that the current is approximately proportional to the square of the voltage, which is in good accordance with the SCLC model. When the voltage exceeds 0.5 V (threshold voltage), the injected carriers increase exponentially, which leads to the increase of current exponentially as $I-V^{\alpha}$ (α =175.3) in stage III. During the process, the carriers are transferred from the PVP to the BQDs and captured by the BQDs, which is ascribed to the lower energy level of BQDs (band gap = 2.46 eV) than PVP (band gap = 3.4 eV) and a lower free-carrier concentration than the trapped one caused by the BQDs, similar to the carrier transfer in the BPQD-based device.[36] Subsequently, the curve of $\ln(I)$ vs $\ln(V)$ is in accordance with the Ohmic behavior (slope 1.06) in stage IV when the applied voltage is higher than the switching voltage (Figure 4c) suggests that the current has a nearly positive correlation to the applied voltage. The charges will be again detrapped as the negative voltage is applied, and the built-in electrical field will disappear (stage VI). Therefore, the memory device returns to the LCS, and the erasing/resetting operation of the device is carried out.

https://dx.doi.org/10.1021/acsami.9b19648
ACS Appl. Mater. Interfaces 2020, 12, 17669−17675

To probe the stability of the device during the operation, a maintain-time test was implemented in the on and off states. After the testing of 10 min at a reading voltage of 0.1 V, no obvious fluctuation was observed under atmospheric conditions (Figure 4d). An on/off current ratio of approximately 10^3 has been achieved, which would promise a low misreading rate during the operation of the memory device. The device has a good reproducibility, as shown in Figure S10. Importantly, the low transition voltage of 0.5 V is desirable for low-power and low-voltage devices, which is significantly lower than BPQD-PVP (1.2 V),[36] molybdenum disulfide MoS_2-PVP (3.5 V),[42] and poly(vinylcarbazole) (PVK)-carbon nanotube (CNT) (1.8 V)-based diodes.[43] This feature makes it to have potential applications in the advanced memory devices with low-power consumption. Previous studies have demonstrated that the pure PVP devices showed no switching behavior,[40] which indicated that the memory effect in our device could be attributed to the presence of BQDs.

4. CONCLUSIONS

In conclusion, we have successfully prepared large-scale and uniform crystalline semiconductor BQDs from the expanded boron powders in the acetonitrile solvent by high-power probe sonication treatment. The as-synthesized BQDs are 2.46 ± 0.4 nm in lateral size and 2.81 ± 0.5 nm in thickness. The size and crystallinity of the BQDs can be further controlled by different process conditions. A strong quantum confinement effect occurs in the BQDs, which is proved by UV−vis and photoluminescence spectroscopy techniques. It is found that a large blue shift up to 184 nm occurs in the BQDs in comparison with the bulk counterpart, which corresponds to the band gap variation from 1.80 eV for the bulk to 2.46 eV for the BQDs. The quantum size effect would render an important alternative for the BQDs as the material for charge trapping in the advanced memory devices. The fabricated BQD-based device shows a rewriteable nonvolatile memory effect with a low switching voltage of only 0.5 V and electrically bistable behavior with an on/off switching ratio of more than 10^3. The synthesis of the BQDs compensates for zero-dimensional vacancies of crystalline boron experimentally; meanwhile, this finding would pave the novel avenues for the 0D crystalline boron quantum dots in highly efficient and high-performance photonic, sensing, and memory devices.

■ ASSOCIATED CONTENT

Supporting Information

The Supporting Information is available free of charge at https://pubs.acs.org/doi/10.1021/acsami.9b19648.

SEM, TEM, XPS, UV−vis, time-resolved PL, and XRD analyses; SEM and TEM images of the expanded boron powder; TEM images of the BQDs; optical property of the bulk boron; time-resolved PL spectra of the boron powder and the BQDs; and XRD spectrum of the boron powder (PDF)

■ AUTHOR INFORMATION

Corresponding Authors

Guoan Tai − *The State Key Laboratory of Mechanics and Control of Mechanical Structures, Laboratory of Intelligent Nano Materials and Devices of Ministry of Education, College of Aerospace Engineering, Nanjing University of Aeronautics and Astronautics, Nanjing 210016, China;* orcid.org/0000-0002-9416-3753; Email: taiguoan@nuaa.edu.cn

Wanlin Guo − *The State Key Laboratory of Mechanics and Control of Mechanical Structures, Laboratory of Intelligent Nano Materials and Devices of Ministry of Education, College of Aerospace Engineering, Nanjing University of Aeronautics and Astronautics, Nanjing 210016, China;* orcid.org/0000-0001-6665-6924; Email: wlguo@nuaa.edu.cn

Authors

Jinqian Hao − *The State Key Laboratory of Mechanics and Control of Mechanical Structures, Laboratory of Intelligent Nano Materials and Devices of Ministry of Education, College of Aerospace Engineering, Nanjing University of Aeronautics and Astronautics, Nanjing 210016, China*

Jianxin Zhou − *The State Key Laboratory of Mechanics and Control of Mechanical Structures, Laboratory of Intelligent Nano Materials and Devices of Ministry of Education, College of Aerospace Engineering, Nanjing University of Aeronautics and Astronautics, Nanjing 210016, China*

Rui Wang − *The State Key Laboratory of Mechanics and Control of Mechanical Structures, Laboratory of Intelligent Nano Materials and Devices of Ministry of Education, College of Aerospace Engineering and School of Material Science and Technology, Nanjing University of Aeronautics and Astronautics, Nanjing 210016, China*

Chuang Hou − *The State Key Laboratory of Mechanics and Control of Mechanical Structures, Laboratory of Intelligent Nano Materials and Devices of Ministry of Education, College of Aerospace Engineering, Nanjing University of Aeronautics and Astronautics, Nanjing 210016, China*

Complete contact information is available at: https://pubs.acs.org/10.1021/acsami.9b19648

Author Contributions

G.T. designed the project, and J.H. performed the experiments with help from R.W. and C.H., who synthesized the samples and performed measurements. J.H. and G.T. carried out data analyses and wrote the manuscript. All authors contributed to discussions and commented on the manuscript.

Notes

The authors declare no competing financial interest.

■ ACKNOWLEDGMENTS

This work was supported by the National Natural Science Foundation of China (61774085 and 51535005), the Six Talent Peaks Project in Jiangsu Province (XCL-046), the Fundamental Research Funds for the Central Universities (NE2017101), and the Priority Academic Program Development of Jiangsu Higher Education Institutions.

■ REFERENCES

(1) Albert, B.; Hillebrecht, H. Boron: Elementary Challenge for Experimenters and Theoreticians. *Angew. Chem., Int. Ed.* **2009**, *48*, 8640−8668.

(2) Akopov, G.; Yeung, M. T.; Kaner, P. B. Rediscovering the Crystal Chemistry of Borides. *Adv. Mater.* **2017**, *29*, No. 1604506.

(3) Sergeeva, A. P.; Popov, I. A.; Piazza, Z. A.; Li, W. L.; Romanescu, C.; Wang, L. S.; Boldyrev, I. S. Understanding Boron through Size-Selected Clusters: Structure, Chemical Bonding, and Fluxionality. *Acc. Chem. Res.* **2014**, *47*, 1349−1358.

(4) Ogitsu, T.; Schwegler, E.; Galli, G. B-Rhombohedral Boron: At the Crossroads of the Chemistry of Boron and the Physics of Frystration. *Chem. Rev.* **2013**, *113*, 3425−3429.
(5) Parakhonskiy, G.; Dubrovinskaia, N.; Dubrovinsky, L.; Mondal, S.; Smaalen, S. High Pressure of Single Crystals of α-Boron. *J. Cryst. Growth* **2011**, *321*, 162−166.
(6) Zarechnay, E.; Dubrovinskaia, N.; Dubrovinsky, L.; Fillinchuk, Y.; Chernyshov, D.; Dmitriev, V. Growth of Single Crystals of B_{28} at High Pressures and High Temperatures. *J. Cryst. Growth* **2010**, *312*, 3388−3394.
(7) Sun, X.; Liu, X.; Yin, J.; Yu, J.; Li, Y.; Hang, Y.; Zhou, X.; Yu, M.; Li, J.; Tai, G.; Guo, W. Two-Dimensional Boron Crystals: Structural Stability, Tunable Properties, Fabrications and Applications. *Adv. Funct. Mater.* **2017**, *27*, No. 1603300.
(8) Mannix, A. J.; Zhang, Z.; Guisinger, N. P.; Yakobson, B. I.; Hersam, M. C. Borophene as a Prototype for Synthetic 2D Materials Development. *Nat. Nanotechnol.* **2018**, *13*, 444−450.
(9) Zhang, Z.; Penev, E. S.; Yakobson, B. I. Two-Dimensional Boron: Structures, Properties and Applications. *Chem. Soc. Rev.* **2017**, *46*, 6746−6763.
(10) Zhang, Z.; Penev, E. S.; Yakobson, B. I. Two-Dimensional Materials: Polyphony in B Flat. *Nat. Chem.* **2016**, *8*, 525−527.
(11) Wu, X.; Dai, J.; Zhao, Y.; Zhuo, Z.; Zhuo, Z.; Yang, J.; Zeng, X. Two-Dimensional Boron Monolayer Sheets. *ACS Nano* **2012**, *6*, 7443−7453.
(12) Zhang, Z.; Yang, Y.; Gao, G.; Yakobson, B. I. Two-Dimensional Boron Monolayers Mediated By Metal Substrates. *Angew. Chem., Int. Ed.* **2015**, *54*, 13022−13026.
(13) Tai, G.; Hu, T.; Zhou, Y.; Wang, X.; Kong, J.; Zeng, T.; You, Y.; Wang, Q. Synthesis of Atomically Thin Boron Films on Copper Foils. *Angew. Chem., Int. Ed.* **2015**, *54*, 15473−15477.
(14) Mannix, A.; Zhou, X.; Kiraly, B.; Wood, J.; Alducin, D.; Myers, B.; Liu, X.; Fisher, B.; Santiago, U.; Guest, J.; Yacaman, M.; Ponce, A.; Oganov, A.; Hersam, M.; Guisinger, P. Synthesis of Borophenes: Anisotropic, Two-dimensional Boron Polymorphs. *Science* **2015**, *350*, 1513−1516.
(15) Feng, B.; Zhang, J.; Zhong, Q.; Li, W.; Li, S.; Li, H.; Cheng, P.; Meng, S.; Chen, L.; Wu, K. Experimental Realization of Two-Dimensional Boron Sheets. *Nat. Chem.* **2016**, *8*, 563−568.
(16) Liu, X.; Zhang, Z.; Wang, L.; Yakobson, B. I.; Hersam, M. C. Intermixing and Periodic Self-Assembly Of Borophene Line Defects. *Nat. Mater.* **2018**, *17*, 783−788.
(17) Wu, R.; Drozdov, I. K.; Eltinge, S.; Zahl, P.; Ismail-Beigi, S.; Bozovic, I.; Gozar, A. Large-Area Single-Crystal Sheets of Borophene on Cu (111) Surfaces. *Nat. Nanotechnol.* **2019**, *14*, 44−49.
(18) Kroto, H. W.; Heath, J. R.; Brien, S. C.; Curl, R. F.; Smalley, R. E. C_{60}: Buckminsterfullerene. *Nature* **1985**, *318*, 162−163.
(19) Wang, H.; Lee, H.-W.; Deng, Y.; Lu, Z.; Hsu, P.; Liu, Y.; Lin, D.; Cui, Y. Bifunctional Non-Noble Metal Oxide Nanoparticle Electrocatalysts Through Lithium-Induced Conversion for Overall Water Splitting. *Nat. Commun* **2015**, *6*, No. 7261.
(20) Bao, J.; Bawendi, M. G. A Colloidal Quantum Dot Spectrometer. *Nature* **2015**, *523*, 67−70.
(21) Ding, Z.; Quinn, B. M.; Haram, S. K.; Pell, L. E.; Korgel, B. A.; Bard, A. J. Electrochemistry and Electrogenerated Chemiluminescence from Silicon Nanocrystal Quantum Dots. *Science* **2002**, *296*, 1293−1297.
(22) Nagaoka, Y.; Tan, R.; Li, R.; Zhu, H.; Eggert, D.; Wu, Y. A.; Liu, Y.; Wang, Z.; Chen, O. Superstructures Generated From Truncated Tetrahedral Quantum Dots. *Nature* **2018**, *561*, 378−382.
(23) BraumanJ. I, J. I. Clusters. *Science* **1996**, *271*, 889.
(24) Kiran, B.; Bulusu, S.; Zhai, H. J.; Yoo, S.; Zeng, X. C.; Wang, L. S. Planar-To-Tubular Structural Transition in Boron Clusters: B_{20} as the Embryo of Single-Walled Boron Nanotubes. *Proc. Natl. Acad. Sci. U.S.A.* **2005**, *102*, 961−964.
(25) Zhai, H. J.; Kiran, B.; Li, J.; Wang, L. S. Hydrocarbon Analogues of Boron Clusters-Planarity, Aromaticity and Antiaromaticity. *Nat. Mater.* **2003**, *2*, 827−833.
(26) Li, W. L.; Chen, Q.; Tian, W. J.; Bai, H.; Zhao, Y. F.; Hu, H. S.; Li, J.; Zhai, H. J.; Li, S. D.; Wang, L. S. The B_{35} Cluster with a Double-Hexagonal Vacancy: A New and More Flexible Structural Motif for Borophene. *J. Am. Chem. Soc.* **2014**, *136*, 12257−12260.
(27) Oger, E.; Crawford, N. R.; Kelting, R.; Weis, P.; Kappes, M. M.; Ahlrichs, R. Boron Cluster Cations: Transition from Planar to Cylindrical Structures. *Angew. Chem., Int. Ed.* **2007**, *46*, 8503−8506.
(28) Piazza, Z. A.; Hu, H. S.; Li, W. L.; Zhao, Y. F.; Li, J.; Wang, L. S. Planar Hexagonal B_{36} as A Potential Basis for Extended Single-Atom Layer Boron Sheets. *Nat. Commun.* **2014**, *5*, No. 3113.
(29) Zhai, H. J.; Zhao, Y. F.; Li, W. L.; Chen, Q.; Bai, H.; Hu, H. S.; Piazza, Z. A.; Tian, W. J.; Lu, H. G.; Wu, Y. B.; Mu, Y. W.; Wei, G. F.; Liu, Z. P.; Li, J.; Li, S. D.; Wang, L. S. Observation of an All-Boron Fullerene. *Nat. Chem.* **2014**, *6*, 727−731.
(30) Qian, W.; Hao, R.; Hou, Y.; Tian, Y.; Shen, C.; Gao, H.; Liang, X. Solvothermal-Assisted Exfoliation Process to Produce Graphene with High Yield and High Quality. *Nano Res.* **2009**, *2*, 706−712.
(31) Li, H.; Jing, L.; Liu, W.; Lin, J.; Tay, R. Y.; Tsang, S. H.; Teo, E. H. T. Scalable Production of Few-Layer Boron Sheets by Liquid-Phase Exfoliation and Their Superior Supercapacitive Performance. *ACS Nano* **2018**, *12*, 1262−1272.
(32) Xu, S.; Li, D.; Wu, P. One-Pot, Facile, and Versatile Synthesis of Monolayer MoS_2/WS_2 Quantum Dots as Bioimaging Probes and Efficient Electrocatalysts for Hydrogen Evolution. *Adv. Funct. Mater.* **2015**, *25*, 1127.
(33) Liu, M.; Xu, Y.; Wang, Y.; Chen, X.; Ji, X.; Niu, F.; Song, Z.; Liu, J. Boron Nitride Quantum Dots with Solvent-Regulated Blue/Green Photoluminescence and Electrochemiluminescent Behavior for Versatile Applications. *Adv. Opt. Mater.* **2017**, *5*, No. 1600661.
(34) Li, H.; Tay, R. Y.; Tsang, S. H.; Zhen, X.; Teo, E. H. Controllable Synthesis of Highly Luminescent Boron Nitride Quantum Dots. *Small* **2015**, *11*, 6491−6499.
(35) Werheit, H.; Filipov, V.; Kuhlmann, U.; Schwarz, U.; Armbruster, M.; Leithe-Jasper, A.; Tanaka, T.; Higashi, I.; Lundstrom, T.; Gurin, V. N.; Korsukova, M. M. Raman Effect in Icosahedral Boron-Rich Solids. *Sci. Technol. Adv. Mater.* **2010**, *11*, No. 023001.
(36) Zhang, X.; Xie, H.; Liu, Z.; Tan, C.; Luo, Z.; Li, H.; Lin, J.; Sun, L.; Chen, W.; Xu, Z.; Xie, L.; Huang, W.; Zhang, H. Black Phosphorus Quantum Dots. *Angew. Chem., Int. Ed.* **2015**, *54*, 3653−3657.
(37) Ji, X.; Kong, N.; Wang, J.; Li, W.; Xiao, Y.; Gan, S. T.; Zhang, Y.; Li, Y.; Song, X.; Xiong, Q.; Shi, S.; Li, Z.; Tao, W.; Zhang, H.; Mei, L.; Shi, J. A Novel Top-Down Synthesis of Ultrathin 2D Boron Nanosheets for Multimodal Imaging-Guided Cancer Therapy. *Adv. Mater.* **2018**, *30*, No. 1803031.
(38) Tauc, J.; Grigorovici, R.; Vancu, A. Optical Properties and Electronic Structure of Amorphous Germanium. *Phys. Status Solidi* **1966**, *15*, 627−637.
(39) Liu, F.; Jang, M. H.; H, H. D.; Kim, J. H.; Cho, Y. H.; Seo, T. S. Facile Synthetic Method for Pristine Graphene Quantum Dots and Graphene Oxide Quantum Dots: Origin of Blue and Green Luminescence. *Adv. Mater.* **2013**, *25*, 3657−3662.
(40) Paul, S.; Kanwal, A.; Chhowalla, M. Memory Effect in Thin Films of Insulating Polymer and C_{60} Nanocomposites. *Nanotechnology* **2006**, *17*, 145−149.
(41) Zhuang, X. D.; Chen, Y.; Liu, G.; Li, P. P.; Zhu, C. X.; Kang, E. T.; Noeh, K. G.; Zhang, B.; Zhu, J. H.; Li, Y. X. Conjugated-Polymer-Functionalized Graphene Oxide: Synthesis and Nonvolatile Rewritable Memory Effect. *Adv. Mater.* **2010**, *22*, 1731−1735.
(42) Liu, J.; Zeng, Z.; Cao, X.; Lu, G.; Wang, L. H.; Fan, Q. L.; Huang, W.; Zhang, H. Preparation of MoS_2-Polyvinylpyrrolidone Nanocomposites for Flexible Nonvolatile Rewritable Memory Devices with Reduced Graphene Oxide Electrodes. *Small* **2012**, *8*, 3517−3522.
(43) Liu, G.; Ling, Q. D.; Teo, E. Y.; Zhu, C. X.; Chan, D. S.; Neoh, K. G.; Kang, E. T. Electrical Conductance Tuning and Bistable Switching in Poly(N-vinylcarbazole)-Carbon Nanotube Composite Films. *ACS Nano* **2009**, *3*, 1929−1937.

https://dx.doi.org/10.1021/acsami.9b19648
ACS Appl. Mater. Interfaces 2020, 12, 17669−17675